

From bulk to interface: solvent exchange dynamics and their role in ion transport
and the interfacial model of rechargeable magnesium batteries

Ying Chen^{a‡}, Rasha Atwi^{b‡}, Dan Thien Nguyen^{a‡}, J. David Bazak^a, Nathan T. Hahn^c, Jaegeon Ryu^{ad}, Jesse A. Sears^c, Kee Sung Han^a, Minyung Song^a, Zheng Li^a, Abhijeet J. Karkamkar^a, Jian Zhi Hu^a, Kevin R. Zavadil^c, Nav Nidhi Rajput^b, Karl T. Mueller^{a*}, Vijayakumar Murugesan^{a*}

^aJoint Center for Energy Storage Research (JCESR), Pacific Northwest National Laboratory, Richland, WA 99352, USA

^bDepartment of Materials Science and Chemical Engineering, Stony Brook University, Stony Brook, New York 11794, USA

^cJoint Center for Energy Storage Research (JCESR), Material, Physical and Chemical Sciences Center, Sandia National Laboratories, Albuquerque, New Mexico 87185, USA

^dDepartment of Chemical and Biomolecular Engineering, Sogang University, Seoul, 04107 Republic of Korea

^eEnvironmental Molecular Sciences Laboratory, Pacific Northwest National Laboratory, Richland, WA 99352, USA

* To whom correspondence may be addressed. Email: Karl.Mueller@pnnl.gov; Vijay@pnnl.gov.

‡These authors contribute equally.

The authors declare no competing interest.

Abstract

Multivalent battery chemistries have been explored in response to the increasing demand for high-energy rechargeable batteries utilizing sustainable resources. Solvation structures of working cations have been recognized as a key component in the design of electrolytes; however, most structure–property correlations of metal ions in organic electrolytes usually build upon favorable static solvation structures, often overlooking solvent exchange dynamics. We report here the ion solvation structures and solvent exchange rates of magnesium electrolytes in various solvents using multimodal NMR analysis and MD/DFT calculations. These magnesium solvation structures and solvent exchange dynamics are correlated to the combined effects of several physicochemical properties of the solvents. Moreover, Mg^{2+} transport and interfacial charge transfer efficiency are found to be closely correlated to the solvent exchange rate in the binary electrolytes where the solvent exchange is tunable by the fraction of diluent solvents. Our primary findings are (1) most battery-related solvents undergo ultraslow solvent exchange coordinating to Mg^{2+} (with time scales ranging from 0.5 μs to 5 ms), (2) the cation transport mechanism is a mixture of vehicular and structural diffusion even at the ultraslow exchange limit (with faster solvent exchange leading to faster cation transport), and (3) an interfacial model wherein organic-rich regions facilitate desolvation and inorganic regions promote Mg^{2+} transport is consistent with our NMR, electrochemistry, and cryo-XPS results. This observed ultraslow solvent exchange and its importance for ion transport and interfacial properties necessitates the judicious selection of solvents and informed design of electrolyte blends for multivalent electrolytes.

Introduction

The solvation process of ions in bulk electrolytes and at liquid–liquid or liquid–solid interfaces is a ubiquitous phenomenon across the scientific domains of electrochemistry, geochemistry,

biochemistry, catalysis, separations, energy conversion/storage, and beyond. Metal-ion solvation structure in electrolytes and at the electrolyte-electrode interface has recently been recognized as a key component affecting battery performance.¹⁻⁵ Successful manipulation of the solvation structure has been realized in Li⁺, Na⁺, K⁺, Mg²⁺, and Zn²⁺ batteries to achieve enhanced oxidative stability, better safety, higher energy density, and longer lifetimes.⁵⁻¹⁰ Engineering the electrolyte solvation structure is considered an even more important factor in battery design than controlling the solid-electrolyte interphase (SEI) in some recent studies.¹¹ However, most structure–property correlations of metal ions reported in the literature are usually based on static solvation structures, such as the composition of the anion and solvent in the first solvation shell based on thermodynamic parameters. Although this solvation structure may be readily obtained from Raman spectroscopy,¹²⁻¹³ nuclear magnetic resonance (NMR),¹⁴ X-ray pair distribution function,¹⁵ and single-crystal X-ray diffraction (SCXRD)¹⁶⁻¹⁷ of crystals grown from saturated electrolytes, this static picture is merely a snapshot of the complex dynamic processes that govern the molecular-scale behavior of electrolytes and furnishes limited inference about the ramifications of these processes for macroscale materials and battery-level performance.

Solvation dynamics, which is the reorganization of solvent molecules around a suddenly introduced charged probe, occurs on timescales ranging from less than 50 fs (vibration and rotational relaxation) to hundreds of ps or even longer (reorientation or translation of solvents around a solute).¹⁸ Out of all solvent motions, solvent exchange dynamics – described by the rate at which a solvent molecule moves out of or into the first solvation shell – is positioned to play a critical role in affecting the ion transport in bulk electrolytes, the desolvation process, and the charge transfer at the electrolyte/electrode interface.¹¹ However, although water exchange and ligand substitution reactions at metal centers have been widely explored,¹⁹⁻²⁴ solvent exchange

dynamics of the organic solvents that are relevant to multivalent battery chemistries is rarely reported.

Ultrafast two-dimensional infrared (2D IR) spectroscopy has been recently employed to examine a series of electrolytes consisting of metal (Li^+ , Mg^{2+} , Zn^{2+} , Ca^{2+} , and Ba^{2+}) bis(trifluoromethylsulfonyl)imide (TFSI) salts in acetonitrile (ACN), and from these studies the lower experimental boundary for the residence times of ion-coordinating solvent molecules in the cation solvation shell is placed at several hundred picoseconds, due to the limit of the temporal window for 2D IR probing.²⁵ In contrast to 2D IR, which can detect solvent exchange at the fast limit, NMR has been more widely utilized to study solvent exchange at the intermediate and slow limits. Our previous studies on MgTFSI_2 in 1,2-dimethoxyethane (DME) show that Mg^{2+} ions form fully solvated clusters $[\text{Mg}(\text{DME})_3]^{2+}$ at concentrations equal to or greater than 0.1 M and the residence time of bound DME spans the range of a few tenths of a millisecond to hundreds of milliseconds, depending on salt concentration and temperature.²⁶⁻²⁷ Therefore, due to the extremely long residence time of DME with Mg^{2+} cations, we use it as a baseline in the first task of this study: we prepare a variety of mixed-solvent electrolytes by maintaining a MgTFSI_2 : DME molar ratio of 1:3 with a wide range of cosolvents added with the goal of determining their solvation power and solvent exchange rate relative to DME. The cosolvents include fluorinated ethers, carbonates, sulfones, phosphates, and nitrogen-containing solvents such as ACN and 2-methoxyethylamine (MEA) as these cosolvents are often utilized in engineered electrolyte systems. With the solvation structures, solvent exchange rates and the activation barriers of exchange in these MgTFSI_2 -3DME-cosolvent systems obtained using NMR and molecular dynamics (MD) and density functional theory (DFT) calculations, we establish connections among solvation structures, exchange dynamics and several typical solvent physiochemical properties

(solvent donor number, relative permittivity, viscosity, coordination asymmetry and steric constraints).

Examination of ion transport usually involves two distinct molecular mechanisms: vehicular transport, wherein a tightly associated solvation shell diffuses as a whole, and structural diffusion, where the ions hop among solvents rapidly (or more precisely, the ions switch their coordinating solvents before they have diffused the length of a solvation shell). Therefore, comparison between the diffusion length which occurs within the residence time of a coordinating solvent (τ_{res}) and the characteristic size of a solvation shell can be used to distinguish between the two diffusion mechanisms. However, the manner in which solvent exchange enters this picture of contrasting ion diffusion mechanisms is still not fully understood. Consequently, the second goal of this study, along a complementary axis to our first goal, is to illustrate this effect on magnesium ion diffusion in a series of MgTFSI₂-DME-MEA electrolytes, where the exchange rate of coordinating MEA can be adjusted by the fraction of DME.

In addition to the impact on ion diffusion and bulk electrolyte properties, the utilization of specific ion solvation structures has been shown to enable compositional design of the solid electrolyte interphase (SEI). After ions diffuse to the surface of the anode, before adsorption and electron transfer take place, ion desolvation has been previously proposed as a key step in the interfacial dynamics of Li batteries, as described in solvation structure-derived interfacial models.^{11, 28-31} Enhanced battery performance has been reported by regulating this desolvation process of metal cations using superconcentrated electrolytes on the liquid side of the interface or metal-organic framework (MOF) materials on the solid side³², both of which facilitate partial desolvation in advance of the ion directly reaching the interface. However, the desolvation process seems to be bypassed in Mg and Ca batteries, with solvent reorganization occurring directly during electron

transfer to the fully solvated ions.¹⁰ Therefore, our third focus in this study is to correlate charge transfer efficiency and solvent exchange dynamics in MgTFSI₂-DME-MEA electrolytes based on our NMR, cryogenic XPS (cryo-XPS), and electrochemistry analyses. Achievement of this goal enables our proposal of a generalized interfacial model for electrodeposition/dissolution at the magnesium anode.

Results and Discussions

In the MgTFSI₂-3DME-cosolvent electrolytes in our study (sample preparation procedures shown in SI, Table S1 – S2), the cosolvent structure classes range from long-chain ethers to cyclic ethers and fluorinated ethers, along with carbonates, sulfones, phosphates, and nitrogen-containing solvents (Figure 1A). The long-chain ethers selected were dipropyl ether (DPE) and dibutyl ether (DBE). The cyclic ethers were tetrahydrofuran (THF) and 2-methyltetrahydrofuran (MeTHF). The fluorinated ethers consisted of 1,1,2,2-tetrafluoroethyl-2,2,3,3-tetrafluoropropyl ether (TTE) and bis(2,2,2-trifluoroethyl) ether (BTFE). For carbonate cosolvents, propylene carbonate (PC), dimethyl carbonate (DMC) and ethyl methyl carbonate (EMC) were chosen. One sulfone – ethyl isopropyl sulfone (EiPS) – and one phosphate – triethyl phosphate (TEP) – were included in this study, and the remaining candidates were nitrogen-containing solvents: ACN, MEA, and trimethylsilyl imidazole (TMSI). From this set of electrolyte permutations, it was determined that MgTFSI₂-3DME-DPE and -DBE have a solubility less than 0.2 M, while 0.25 – 0.75 M MgTFSI₂-3DME-MeTHF, -DMC and -EMC form a liquid-liquid phase separation boundary, which is described in our previous work.³³ For the remaining ten solutions, we observe a variety of solvation structures and solvent exchange rates dependent on the physiochemical properties of the cosolvent.

NMR analysis of solvation and exchange

Magnesium solvation structures and solvent exchange rates of the mixed-solvent electrolytes were investigated using ^1H , ^{13}C , ^{15}N , ^{17}O , ^{19}F , ^{25}Mg and ^{31}P NMR at varying temperatures. Taking 0.45 M MgTFSI_2 -3DME-THF as an example, ^1H NMR spectra of both DME and THF protons (Figure 1B) display a typical pattern of two-site chemical exchange³⁴ when lowering the temperature from 20 °C to -15 °C: THF resonances become broader until a coalescence point at 0 °C and then sharpened into two distinguishable sets of signals at -15 °C, while the DME peaks appear as broad shoulders at 20 °C which progressively sharpen into three sets of signals as the temperature decreases. Based on our previous work, coordination to Mg^{2+} shifts ^1H signals of bound DME to a higher frequency. Correspondingly, here we assign the two sets of THF signals as bound and free THF, and the three sets of DME signals as bidentate, monodentate, and free DME, from higher to lower frequency. The fraction of each component was calculated directly using quantitative ^1H NMR methodology. Due to the fixed molar ratio of DME: Mg^{2+} at 3.0, we can further calculate that the number of bound and free THF per Mg^{2+} is 4.0 and 14.3, respectively, and that the numbers of bidentate, monodentate, and free DME per Mg^{2+} are 0.2, 0.5, and 2.3 on average, using the line shape analysis tool “Dynamic NMR Models (DNMR)” built in Topspin Bruker with the initial fractions of each component obtained from line fittings of 1D ^1H NMR signals (Figure S1) and the initial exchange rates estimated from the 2D ^1H - ^1H EXSY (Figure 1C) with more details in SI under Experimental methods – NMR data analysis (Figure S2-S5). The exchange rates between the free and bound species can be obtained from the lineshape analysis, with the residence time of bound THF and bound DME (averaging between bidentate and monodentate species) at -15 °C calculated to be 3 and 20 ms, respectively.

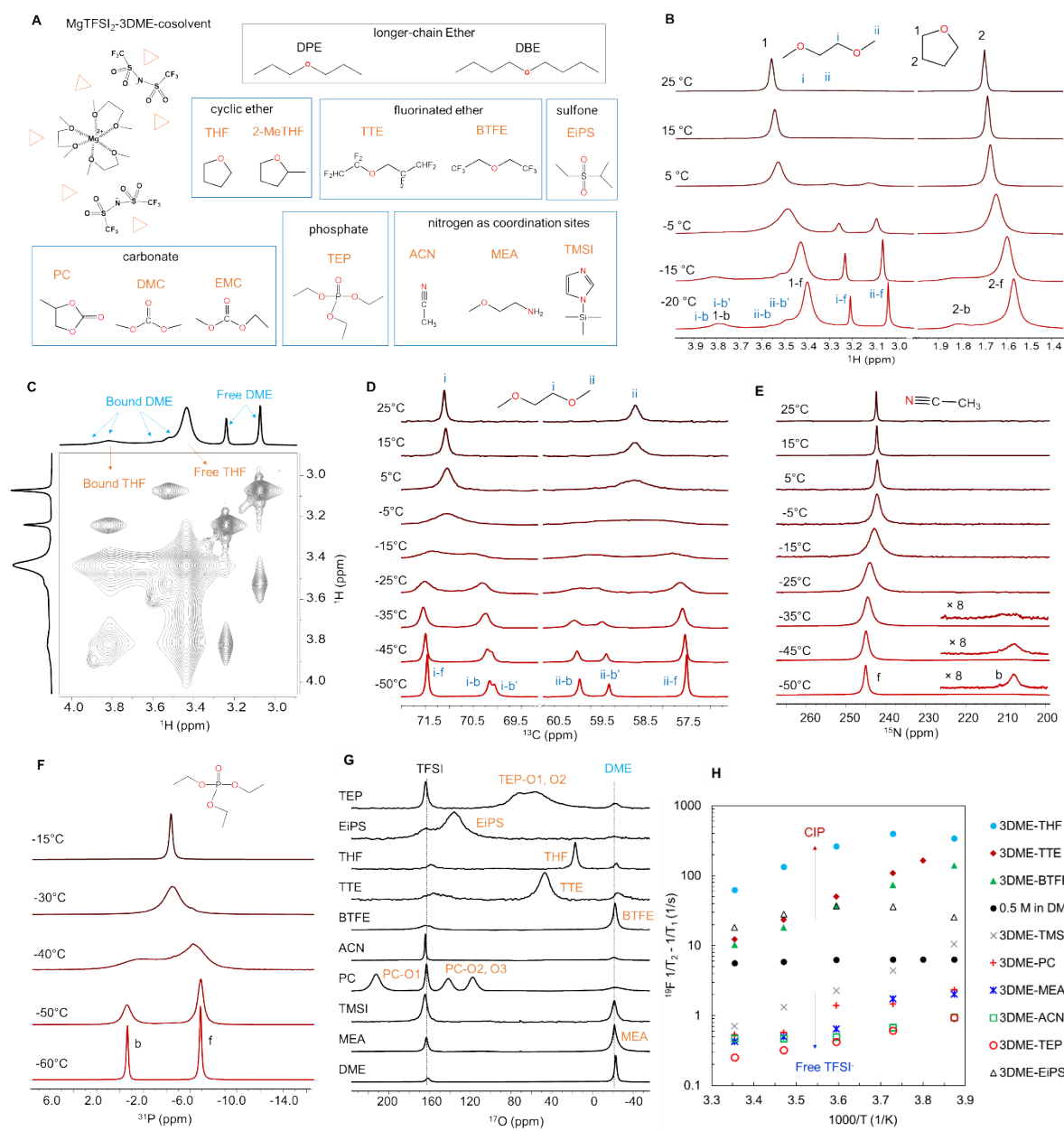


Figure 1. The names and structures of the solvents covered in the MgTFSI_2 -3DME-cosolvent study (A), and a few examples of the NMR spectra used for characterizing ion solvation: (B) ^1H single-pulse NMR spectra and (C) ^1H - ^1H 2D EXSY of 0.45 M MgTFSI_2 -3DME-THF; (D) ^{13}C and (E) ^{15}N NMR spectra of 0.45 M MgTFSI_2 -3DME-ACN (^{15}N -labeled), and (F) ^{31}P NMR spectra of 0.45 M MgTFSI_2 -3DME-TEP. NMR spectra of other solutions are discussed in the SI (Figure S1-

S23). (G) ^{17}O NMR spectra of MgTFSI_2 -3DME-cosolvents at 25 °C. (H) ^{19}F NMR relaxation rate differences ($1/T_2 - 1/T_1$) plotted against the scaled inverse temperature $1000/T$.

While ^1H NMR is the most sensitive, ^{13}C NMR with ^1H decoupling can provide better resolution and less overlap for dynamic line shape analysis.³⁵ For example, the three components of DME are well resolved in the ^{13}C NMR of 0.45 M MgTFSI_2 -3DME-ACN (Figure 1D), and line shape analysis of the spectra at -50 °C shows that the exchange rates from bidentate DME to monodentate, bidentate to free, and monodentate to free are 5.7, 7.2, and 2.6 s^{-1} , respectively. This reveals that bidentate DME can (and does) leave the Mg^{2+} center synchronously without necessarily first passing through monodentate coordination. In the same electrolyte, however, the free and bound ACN species are not resolved in ^{13}C NMR prior to reaching the freezing point at -55 °C. Instead, ^{15}N NMR spectra with ^{15}N -labeled ACN can distinguish the bound from free ACN, with a peak separation of 37.5 ppm occurring for this nucleus (Figure 1E) from which the exchange rate is estimated to be 350 s^{-1} at -50 °C. Other nuclei that are close to the coordinating sites, such as ^{31}P from TEP (Figure 1F), can also be used to extract structural and exchange information for the cosolvents.

Using the chemical shifts and fractions of the bound and free species, as well as the exchange rates between them obtained at the lower temperatures as initial guesses, line shape analysis can estimate the fractions of and exchange rates between the bound and free species at higher temperatures. However, as the fast exchange limit is approached (e.g., by raising the temperature), the intrinsic linewidth of the NMR signal becomes a dominating parameter in line shape analysis and can introduce significant errors into the fitted exchange rates. Accordingly, in our study we use 2D EXSY at the slow exchange limit and line shape analysis at the intermediate exchange range to calculate the exchange rates k_{ex} (corresponding to temperatures between -50 °C and 5 °C for most

samples, refer to Figure S2 – S5 and related discussions for more details). Eyring plots of $\ln(k_{\text{ex}}/T)$ versus the inverse temperature, scaled here as $1000/T$, are used to extract the activation enthalpy ΔH^\ddagger and entropy ΔS^\ddagger using the Eyring formulation $\ln(k_{\text{ex}}/T) = \ln(k_B T/h) - \Delta H^\ddagger/RT + \Delta S^\ddagger/R$.³⁶⁻³⁷ As shown in Figure S21, Eyring plots of $k_{\text{ex}}(\text{DME})$ and $k_{\text{ex}}(\text{cosolvent})$ exhibit good linear relationship ($R^2 > 0.98$). Therefore, the exchange rates at higher temperatures (5 – 25 °C) can be extrapolated from the Eyring plots.

In contrast to these results for the solvents and cosolvents, the TFSI⁻ anions experience the fast-exchange limit in most Mg electrolytes,^{27, 33} so we usually do not observe well-resolved ¹³C, ¹⁷O, or ¹⁹F NMR signals arising from free and bound anions, even at the lowest temperatures before the solutions freeze or nucleate. While Raman spectroscopy has been employed as the major tool to distinguish between free TFSI⁻, solvent-separated ion pairs (SSIPs), and contact ion pairs (CIPs) in these electrolytes, the assignments of these species are still under debate with conflicting reports in literature.^{10, 12, 16, 38} Therefore, in this study we use NMR linewidth and relaxation analysis to qualitatively evaluate the existence of CIPs in a given composition at a given temperature. While the ¹⁷O (Figure 1G) chemical shifts of TFSI⁻ and DME are almost invariant across all the cosolvent combinations, the difference in the signal intensity and linewidth (Figure S18) between TFSI⁻ and DME can reflect the coordination status of TFSI⁻ versus DME. As reported in our previous work, DFT-calculated ¹⁷O signals of the TFSI⁻ and DME coordinating to Mg²⁺ are significantly shifted from the signals of free TFSI⁻ and DME by 64 ppm and 16 ppm, respectively,²⁶ because oxygen atoms are the coordinating sites for both. The facts that the observed ¹⁷O chemical shifts are ± 0.5 ppm within the free species and that they are insensitive to the cosolvents suggest that only ¹⁷O signals of non-coordinating TFSI and DME are detectable. Here the linewidth of ¹⁷O is primarily determined by the quadrupolar relaxation and the chemical exchange between bound and free

species. The quadrupolar relaxation is modulated by the rotation correlation time that is dictated by the solution viscosity and coordination status; oxygens coordinating to Mg^{2+} may experience very fast quadrupolar relaxation, which results in signals too broad to be detected. While we cannot observe the coordinating ^{17}O , the exchange between the free and bound species can cause broadening in the observable ^{17}O signals arising from the free species: a slower exchange leads to a broader signal in the fast-exchange limit relative to the NMR timescale. Therefore, a broader TFSI- ^{17}O signal compared to DME indicates that a higher degree of CIP formation is occurring (more coordinating TFSI- or longer residence time). In addition to these observations, the difference between ^{19}F spin-spin relaxation rate $1/T_2$ and spin-lattice relaxation rate $1/T_1$ can also be used as a qualitative method (Figure 1H). As ^{19}F is located at the terminal CF_3 group of TFSI, the relaxation mechanisms that contribute to both ^{19}F T_1 and T_2 include intra- and inter-molecular dipolar interaction, chemical shift anisotropy, and spin rotation,³⁹ which are modulated by the tumbling reorientation of TFSI and the internal CF_3 rotation; so a slower tumbling motion of TFSI leads to a smaller ^{19}F T_2 compared to T_1 . Furthermore, ^{19}F T_2 is also highly influenced by the chemical exchange rates between multiple sites (bound vs free TFSI) and conformal structures (*cis* vs *trans*). At the fast exchange limit, a slower exchange results in a smaller ^{19}F T_2 compared to T_1 . Therefore, a larger $1/T_2 - 1/T_1$ can be correlated with a greater degree of CIPs which is associated with either more restricted molecular rotation or slower exchange between bound and free TFSI-. In addition, a maximum in $1/T_2 - 1/T_1$ vs temperature observed in the cosolvents with THF and EiPS indicate the start of coalescence of the bound and free TFSI signals. However, we also note that the solution viscosity and its dependence on temperature may have significant effect on ^{19}F T_1 and T_2 that is not fully accounted in $1/T_2 - 1/T_1$, therefore we only use it for qualitative evaluation of CIP formation. 3DME-THF and 3DME-EiPS are the only solutions that exhibit the transition

of TFSI⁻ from fast to slow exchange as temperature lowers from 25 °C to -25 °C (Figure S19). Combining the observations from the ¹⁷O, ¹⁹F, and ¹³C NMR spectra of TFSI⁻, we conclude that a significant degree of CIP formation is present in the electrolyte mixtures with the cosolvent THF, EiPS, TTE, and BFTE (consistent with the previous study on the fluorinated solvents)⁴⁰, while TFSI⁻ mostly exists as free anions in the MEA, TEP, PC and ACN solutions.

Solvation structures

Table 1 summarizes the overall findings regarding the Mg²⁺ solvation structures – coordination number of DME and cosolvent, along with the presence or absence of CIP in the 0.45 M MgTFSI₂-3DME-cosolvent mixtures. These solvation structures can be categorized into three types: a) only DME coordinates to Mg²⁺ and the cosolvents behave as free solvents (TTE and BTFE); b) both DME and the cosolvent coordinate to Mg²⁺, albeit with different coordination numbers (THF, PC, EiPS, and ACN); or c) only the cosolvent coordinates to Mg²⁺ while all of the DME molecules are pushed out of the first solvation shell (TMSI, TEP, and MEA).

Table 1. Summary of Mg²⁺ solvation structure (number of bound and free solvent per Mg²⁺ and formation of stable CIP) and solvent exchange dynamics (residence time of bound DME and bound cosolvent) at -15 °C in 0.45 M MgTFSI₂-3DME-cosolvent.

Cosolvent	Bidentate DME per Mg ²⁺	Monodentate DME per Mg ²⁺	Free DME per Mg ²⁺	Bound cosolvent per Mg ²⁺	Free cosolvent per Mg ²⁺	Residence time of bound DME (ms)	Residence time of bound cosolvent (ms)	“Stable” CIP with TFSI
DME	3.0	0	15.0	0	0	250	-	No
THF	0.2	0.5	2.5	4.0	14.3	20	3	Yes
PC	1.0	0.5	1.5	3.0	14.5	6.0	0.7	No
EiPS		1.8	1.2	1.9	10.4	65	11	Yes
ACN	0.8	0.7	1.5	3	25.5	2.4	0.06	No
TEP	0	0	3.0	6.2	4.5	-	0.03	No
MEA	0	0	3.0	5.2	16.0	-	0.06	No
TMSI	0	0	3.0	6.1	5.3	-	25	No
TTE	2.0	0.7	0.3	0	10.4	110	-	Yes
BTFE	2.1	0.6	0.3	0	12.5	80	-	Yes

In order to understand how the solvent physicochemical properties affect ion solvation of the mixed-solvent systems, we compile measurements of some common physicochemical properties of the solvents, including Gutmann’s donor number, relative permittivity, viscosity, density, and molar volume in Table S2. It is immediately obvious that the coordination number of the solvents is directly correlated to the solvent’s donor number (Figure 2A and 2B). For example, the donor numbers of THF, PC, EiPS and ACN are between 14 and 20, comparable to that of DME (donor number of 20), so this group of cosolvents competes with DME to coordinate to Mg²⁺. THF has the highest donor number of the group and correspondingly exhibits the highest coordination number. On the other hand, the group of cosolvents containing MEA, TEP, and TMSI all have significantly greater donor numbers than DME, therefore they completely replace DME and fully solvate Mg²⁺. At the other end of the donor number range, TTE and BTFE each has a donor number less than 10, and consequently they do not participate in the first solvation shell. Since the solvation structure is mainly determined by the solvation energy ΔG^{sol} , which is the total free energy released

or required to assemble the solvation shell, Gutmann's donor number can be a good proxy metric for ΔG^{sol} . With the caveat that the donor number represents ΔG^{sol} of SbCl_5 in 1,2-dichloroethane,⁴¹ some differences with regards to Mg^{2+} could exist due to the significant contrast in the ion size, charge and electron configuration between Mg^{2+} and Sb^{5+} . Nevertheless, a recent study involving 36 solvents in localized high-concentration electrolytes also reached the similar conclusion that the donor number is an effective design parameter for Li^+ solvation structure.⁴²

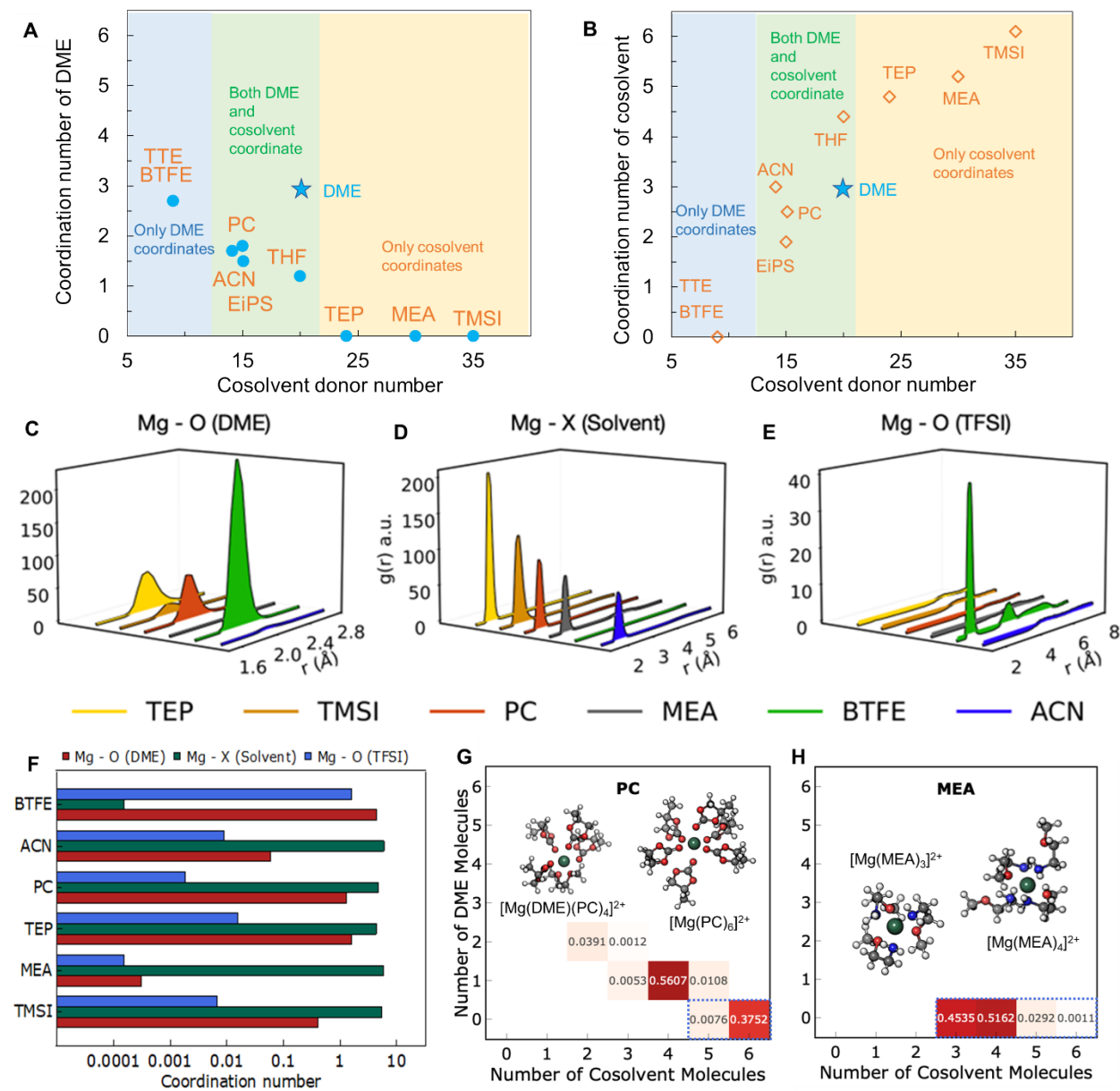


Figure 2. Ion solvation structures of the MgTFSI₂-3DME-cosolvent electrolyte mixtures. Coordination number of bound DME (A) and bound cosolvent (B) is plotted against the cosolvent donor number. Radial distribution functions of (C) Mg - O (DME), (D) Mg - X (Solvent), and (E) Mg - O (TFSI) in 0.45 M Mg(TFSI)₂-3DME-cosolvent²⁺ (TEP, TMSI, PC, MEA, BTFE, ACN). X corresponds to the coordinating site in each cosolvent. (F) Coordination number between Mg - O (DME), Mg - X (Solvent), and Mg - O (TFSI). Stoichiometry probability densities of the solvation

structures in 0.45 M MgTFSI₂-3DME in (G) PC and (H) MEA along with sample solvation structures from each system in ball-and-stick representation.

Solvent donor number is also a determining factor for the formation of CIPs between Mg²⁺ and TFSI⁻: a solvent with high donor number prevents the formation of CIPs, as was the case with the MEA, TEP, and TMSI cosolvent mixtures, whereas a solvent with low donor number allows for stable CIPs, such as in TTE and BFTE combinations. Solvent relative permittivity also plays a key role in the formation of CIPs as well: solvents with high relative permittivity can effectively screen the electrostatic interactions between ions and reduce CIP formation. For example, for the cosolvents with comparable donor number to DME, only free TFSI⁻ are present in PC and ACN due to their higher relative permittivity; CIP forms in THF due to its low relative permittivity; stable CIPs are observed in EiPS which has the second highest permittivity, demonstrating that donor number is a more important factor than relative permittivity in determining the formation of CIP. Another important factor is viscosity: a solvent with a greater viscosity has a lower ion mobility and thereby provides a longer time scale within which the bulky anion TFSI⁻ can bind to Mg²⁺, depending on the ability of the solvents to adequately screen the charges of the ions. EiPS is an exemplar: the extremely high viscosity it possesses prevails over its high relative permittivity and reduces the exchange rate of TFSI⁻ between free and bound species. As shown in Figure S19, the ¹⁹F signal of bound TFSI appears when the temperature decreases to -15 °C and lower. This indicates that the residence time of bound TFSI is on the millisecond scale at these temperatures. Notably, this is the only cosolvent electrolyte examined in this study where we can detect the bound TFSI using ¹⁹F NMR. This suggests that the high viscosity of EiPS allows for the formation of stable CIPs. In other words, viscosity affects the kinetics of anion exchange with a higher viscosity leading to a longer lifetime of CIPs, but viscosity should not affect the thermodynamics

equilibrium of CIP vs free TFSI⁻. Interestingly, if we replace DME with MEA, no CIPs are observed in MgTFSI₂-3MEA-EiPS due to the high solvating power of MEA, again conforming that donor number is the most important factor. Therefore, for a bulky anion with low charge density, the combined effect of solvent donor number, relative permittivity, and viscosity dictates the extent of CIP formation in the mixed-solvent electrolytes (Figure S24).

MD simulations were performed in order to further confirm ion solvation structures in these cosolvent electrolytes. From the radial distribution functions (Figure 2C-E) of Mg – O (DME), Mg – X (cosolvent) with X being the coordinating O or N, and Mg – O (TFSI⁻), the coordination number of the DME, the cosolvent, and the TFSI⁻ can be computed (Figure 2F). The results are in good agreement with the experimental values: DME and TFSI⁻ coordinate to Mg²⁺ when BTFE is the cosolvent; both solvents coordinate in the mixture with PC; and cosolvent coordination dominates with the MEA, TMSI and TEP mixtures. However, the relative degrees of coordination of DME and ACN for the 3DME-ACN mixture differ from the experimental results, with the coordination of ACN overestimated in the simulation results. This probably occurs because the fast ACN mobility and exchange dynamics enable the capture of more intermediate solvation species during the simulation time of 100 ns. The most populated solvation structures in the simulations can also be obtained according to the stoichiometry probability densities. For example, Mg²⁺ coordinating with 4 PC and 1 DME contributes to 56% of all solvation structures in 3DME-PC (Figure 2G), while Mg²⁺ coordinating to 3 or 4 MEA dominates in 3DME-MEA (Figure 2H). Stoichiometry probabilities and most representative structures of other cosolvent systems are discussed in Figure S18 and Table S3 – S8.

Solvation exchange dynamics

Compared to the well-defined static picture of ion solvation structure, it is more complicated to identify the influencing factors for solvent exchange dynamics, which are governed by the activation free energies of exchange ΔG^\ddagger , the small amount of energy variation needed to move a solvent out of and into the first solvation shell. As shown in Figure 3A, the residence time of the bound solvent decreases with the order DME > TMSI ~ EiPS > PC ~ THF > ACN ~ MEA ~ TEP spanning a wide range from 3.5 ms for DME down to 0.5 μ s for TEP (both at 25 °C), while adding a cosolvent to MgTFSI₂-3DME reduces the residence time of bound DME, even with comparatively inert solvents such as BTFE and TTE. To further understand the solvent exchange mechanism, the activation enthalpy ΔH^\ddagger (Figure 3B) and entropy ΔS^\ddagger (Figure 3C) of solvent exchange obtained from the Eyring plots (Figure S15) are compared. Because the measurement of ΔS^\ddagger is highly dependent on the temperature range and prone to experimental errors, we only use ΔS^\ddagger with significantly positive or negative values to identify dissociative activation (D) or associative activation (A), respectively, while ΔS^\ddagger within ± 30 J/mol/K could be interchange (I, I_a or I_d, with bond making and bond breaking being more important in I_a and I_d, respectively), D or A. For the exchange process of cosolvents, the most positive ΔS^\ddagger are 75, 41 and 33 J/mol/K for TEP, TMSI, and THF, respectively, suggesting the D-mechanism with intermediates of reduced coordination number. While the large molar volume of TEP and TMSI can readily explain the D-mechanism activation for those cosolvent mixtures due to the solvent crowding effect at the metal center, a small solvent with a single coordinating site located at a ring structure like THF can also cause remarkable steric hindrance when the metal center is also small, such as with Mg²⁺, and again result in D-mechanism activation. By comparison, PC with a single coordinating site located a bond away from the ring structure has a smaller ΔS^\ddagger due to the reduced steric hindrance at Mg²⁺.

Therefore, solvent bulkiness and coordination steric hindrance are among the most important solvent properties that increase ΔS^\ddagger , thereby reducing ΔG^\ddagger and raising solvent exchange rates. These findings are also consistent with previous reports on ligand substitution reactions for the main group metal ions.^{20-21, 43}

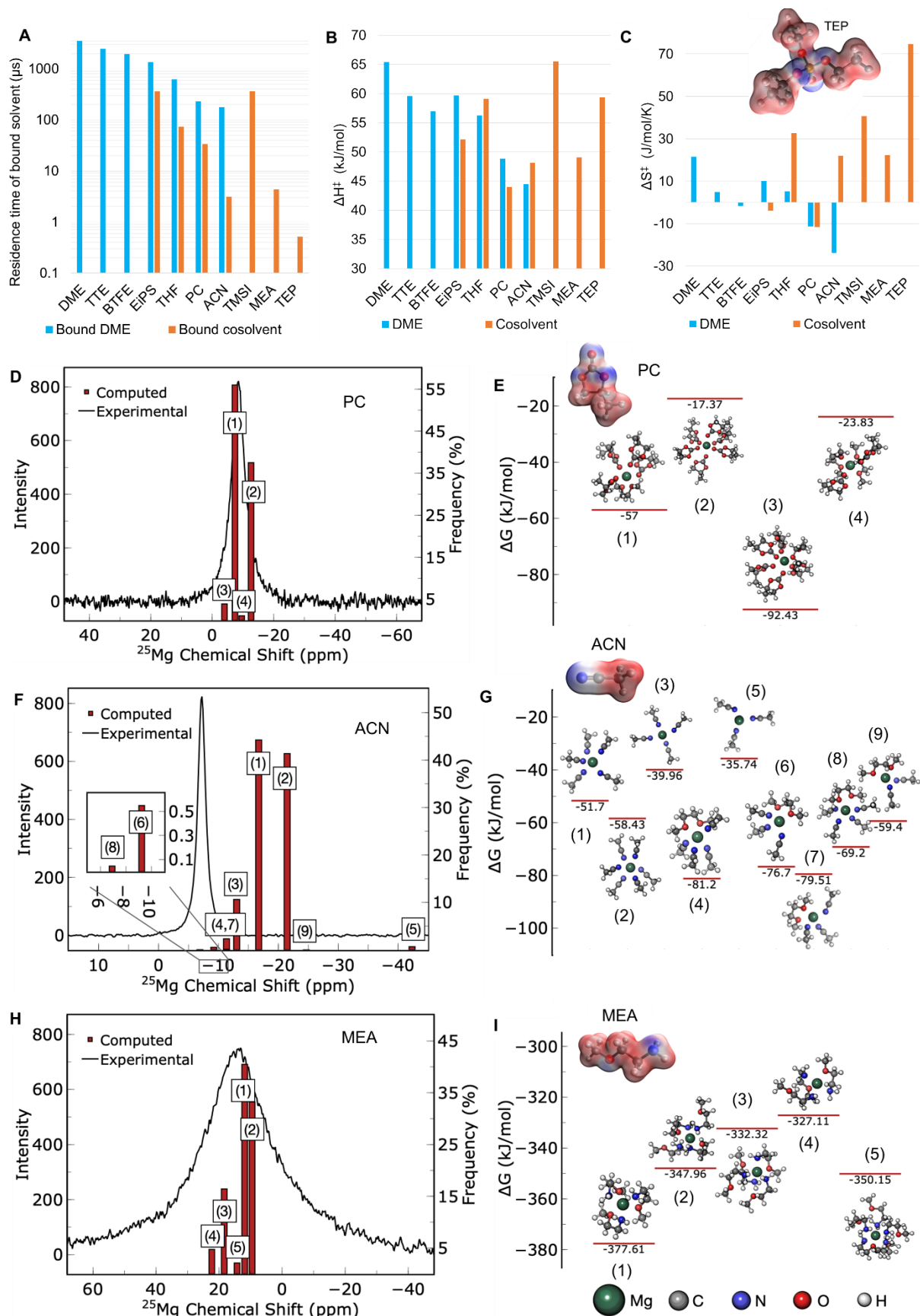


Figure 3. Solvent exchange dynamics and free energy analysis of the MgTFSI₂-3DME-cosolvents. (A) Residence time of bound DME (blue) and bound cosolvent (orange) at 25 °C. (B) Activation enthalpy ΔH^\ddagger and (C) activation entropy of exchange ΔS^\ddagger estimated from the NMR analysis. Experimental and DFT-predicted ²⁵Mg chemical shifts of the most prevalent solvation structures identified in 3DME-PC (D), 3DME-ACN (F) and 3DME-MEA (H), along with the Gibbs free energy of formation of the corresponding structures (E, G, and I). The insets are the electrostatic potential maps of the cosolvent molecules. Refer to Tables S6-S8 for more details about the solvation structures in each system. The absolute error in the computed chemical shift for the top solvation structure is 1.2 ppm, 9.5 ppm, and 1.4 ppm in the PC, ACN, and MEA systems, respectively.

For the solvents that do not exhibit significant size effects, the rate of solvent exchange may be primarily determined by the energetics of metal-ligand bond breaking between Mg²⁺ and the solvent molecules. By comparing ΔH^\ddagger of these solvents along with their properties, it is clear that a single solvent-specific property cannot solely explain the trend. Instead, the combined effects of many solvent properties contribute to ΔH^\ddagger , including solvent rearrangement around the metal center, coordination asymmetry (difference in coordination sites), solvent translational mobility, solvent rotational degrees of freedom, and solvent-solvent interactions. The relatively high ΔH^\ddagger of DME in 0.45 M MgTFSI₂/DME is a result of the rearrangement of DME from multiple flexible configurations in bulk solution to a preferential conformational structure TGT (*trans-gauche-trans*) when coordinating to Mg²⁺. This rearrangement leads to more tight packing of the DME around Mg²⁺ and extremely stable Mg(DME)₃²⁺ clusters. Therefore, the significant decrease in ΔH^\ddagger of DME exchange in MgTFSI₂-3DME-cosolvent electrolytes (Figure 3B) can be explained by the cosolvents perturbing the formation of the Mg(DME)₃²⁺ cluster. This hypothesis is

supported by the solvation structure analysis (Table S1), where both monodentate and bidentate DME are detected with a coordination number less than 3 DME per Mg^{2+} with the presence of cosolvent. Cosolvents with higher donor number, higher relative permittivity, and lower viscosity correspondingly tend to better perturb the Mg^{2+} -DME solvation. The smallest ΔH^\ddagger and most negative ΔS^\ddagger of DME exchange are observed with ACN as the cosolvent, probably because with its extremely low viscosity (high solvent mobility), high relative permittivity and small molar volume, ACN can function as an incoming ligand assistant to the Mg-O (DME) bond breakage process. Even diluents such as BTFE and TTE lower the ΔH^\ddagger of DME exchange (to a greater extent by BTFE, which has a higher relative permittivity and significantly lower viscosity than TTE, as detailed in Table S2).

For solvents with a single coordination site, ΔH^\ddagger follows the order of the solvent donor number, with $\text{TMSI} > \text{TEP} > \text{THF} > \text{ACN} > \text{PC}$. However, amongst solvents with multiple coordination sites, the 16 kJ/mol decrease in ΔH^\ddagger from DME to MEA is surprising, especially considering the almost twofold larger donor number of the amine group in MEA compared to the ether group in DME. Our hypothesis is that the coordination geometry or, more particularly, coordination asymmetry and solvent-solvent interaction may play essential roles in ΔH^\ddagger . When the cation-solvent interaction causes configurational changes in the solvents with multiple coordination sites and lowers the free energy of the solvated clusters, additional energy is required for bond-breaking and ΔH^\ddagger increases accordingly, as in the case of DME. On the other hand, in the case of MEA, which can coordinate to Mg^{2+} using either N or O (with N preferred), the flexible coordination geometry with low symmetry does not introduce a strong electrostriction effect (which would contribute to increasing ΔH^\ddagger). The electrostatic potential maps of the solvent molecules (Figure S19 and Table S9) confirm that the partial charge on MEA is significantly different on the two

sites, with -1.13 on sp^3 nitrogen and -0.51 on sp^3 oxygen. While sp^3 oxygens are also present in PC and TEP with comparable partial charge to sp^2 oxygens (-0.55 and -0.60 on sp^2 O compared to -0.45 and -0.40 on sp^3 O for PC and TEP, respectively), the coordination geometry does not allow both oxygens to serve as coordination sites. Furthermore, interactions that occur beyond the first coordination shell also contribute to ΔH^\ddagger and ΔS^\ddagger . The solvent-solvent interaction is stronger in MEA with intermolecular hydrogen bonding between amine groups, evidenced by its larger viscosity compared to DME (Table S2). MEA in the second coordination sheath may therefore assist the bond breaking between Mg^{2+} and MEA at the first solvation shell and reduce the energy differences for MEA exchange between the first and second coordination shell. Overall, simply changing one of the two ether groups to an amine group leads to a decrease in the residence time from 3.5 ms for DME to 4 μ s for MEA, which is comparable to the residence time of water coordinating to Mg^{2+} (2 μ s) at 25 °C.

MD simulations and DFT calculations are further employed to understand the dynamic features of ion solvation. Using the automated framework we developed for high-throughput predictions of NMR chemical shifts,⁴⁴ 1H , ^{13}C and ^{25}Mg chemical shifts are computed from the most prevalent solvation structures gleaned from the MD simulation snapshots and compared to the experimental values for further confirmation of the assigned solvation structures (Table S10 – S15). Comparing with the experimental spectra, the predominant solvation structures in the electrolytes can be identified. For example, in 0.45 M $MgTFSI_2$ -3DME-PC (Figure 3D), out of four most frequently observed solvation structures from the MD simulations, the experimental ^{25}Mg chemical shift fits well with those of Structures 1 and 4, which correspond to 4 PC and 1 bidentate DME, and 5 PC and 1 monodentate DME (Table S3), respectively, which are consistent with the solvent

coordination number evaluated from NMR. The free energy calculation shows that the energy gap between all four different structures, $\Delta(\Delta G)$, is ~ 75 kJ/mol (Figure 3E).

By contrast, in a second example with MgTFSI₂-3DME-ACN (Figure 3F), the most frequently occurring structures obtained from MD simulations have 5 or 6 coordinating ACN molecules (Structures 1 and 2), but the experimental ²⁵Mg chemical shift agrees with Structures 6 and 8, which have DME and ACN both coordinating to Mg²⁺ (Table S4). While these structures only contribute to less than 1% of the top structures from MD simulations, they are consistent with the coordinating numbers of DME and ACN estimated from the ¹H and ¹³C NMR analyses (Table S1). This discrepancy is because MD simulations are more populated by short-lived clusters due to the relatively short simulation time (5 ns), while NMR acquisition averages over a time scale of milliseconds to seconds, reporting the longer-lived stable solvation structures. The short-lived clusters may reflect the intermediate structures of solvent exchange, and therefore the composite free energy gap between all the structures can be an estimation of ΔG^\ddagger in these cases. Due to the fast mobility of ACN, multiple short-lived structures are present with $\Delta(\Delta G)$ smaller than 45 kJ/mol (Figure 3G). On the other hand, in 0.45 M MgTFSI₂-3DME-MEA, the experimental ²⁵Mg resonance has a linewidth greater than 20 ppm and covers ²⁵Mg chemical shifts calculated from all the most prevalent structures in the MD simulations (Figure 3H). ²⁵Mg NMR spectra measured at different magnetic fields exhibit unaltered isotropic chemical shift and linewidth (Figure S23), indicating that the contribution of quadrupolar broadening due to asymmetric coordination of MEA to Mg²⁺ is neglectable due to the motion averaging. Therefore, the broadness is the result of the co-existence of several solvation structures with 3 to 6 coordinating MEA in the solution. While the formation energies of MEA-coordinating structures are more than three times stronger than those of PC and ACN, the energy gap between the MEA structures is less than 50 kJ/mol (Figure

3I), suggesting a wide distribution of time-averaged states. Therefore, the main conclusion from the MD/DFT calculations (more results in Figure S20-23) is that solvent mobility and coordination asymmetry can significantly raise the likelihood of short-lived clusters forming and the co-existence of various competing solvation structures, which then naturally increases the overall entropy of the solutions and reduces the activation free energy for solvent exchange.

Table S16 compiles the solvent exchange rates of Mg^{2+} with other organic ligands that have been reported in the literature.⁴⁵⁻⁵³ As discussed in some previous reviews, even slight and subtle changes in the solvent coordination sites or geometry can have dramatic impact on the solvent exchange rate and mechanism.^{20-21, 43} Nevertheless, combining with the results in this study, six solvent-related physicochemical properties may have substantial influence in solvent exchange dynamics (Figure S24): greater coordination steric constraints and solvent rotational degree of freedom, larger coordination asymmetry and solvent-solvent interaction, faster solvent motion and smaller solvent rearrangement around metal ions all contribute to faster solvent exchange rates. To directly compare with the reported range of several hundred picoseconds as the lower experimental bound on residence time of Mg-ACN complexes using 2D IR, we performed ^{15}N and ^{13}C NMR on 1 M MgTFSI_2 in ACN. From these measurements, the residence time of coordinating ACN is estimated to be 18 μs at 25 °C (Figure S16), which is 4 – 5 orders of magnitude slower than the lower experimental bound obtained from 2D IR. This slow solvent exchange dynamics, especially for multivalent ions such as Mg^{2+} , Zn^{2+} and Al^{3+} , necessitates a more fundamental understanding about the influence of these dynamics on the bulk and interfacial properties of nonaqueous electrolytes.

Ion transport versus solvent exchange

In order to understand how solvation structure and solvent exchange dynamics influence ion transport and interfacial properties, we choose a binary solvent system consisting of DME and MEA. Due to the greater donor number of the amine moiety, the solvation energy ΔG^{sol} increases from ~ 93.4 kJ/mol for DME to ~ 271 kJ/mol for MEA (refer to SI for donor number measurements details). However, despite possessing nearly tripled the nominal solvation power, MEA exhibits a smaller free energy barrier for solvent exchange (ΔG^\ddagger) of 42 kJ/mol when compared to the value of 59 kJ/mol for DME. Therefore, the free energy profile of the DME solution exhibits a single dominant coordination minimum $\text{Mg}(\text{DME})_3^{2+}$ with a relatively small ΔG^{sol} and a large ΔG^\ddagger for DME exchange (Figure 4A). This contrasts with the MEA solution, for which multiple configurations of $\text{Mg}(\text{MEA})_n^{2+}$ ($n \sim 3 - 6$) are simultaneously present, and which therefore possesses a relatively large ΔG^{sol} and a small ΔG^\ddagger between different configurations (Figure 4B). This multiplicity of the coordination environments has also been previously proposed by free energy analysis using both classical and ab initio molecular dynamics (MD) simulations in aprotic solvents for divalent cations.⁵⁴⁻⁵⁵

In the 0.45 M MgTFSI_2 -DME-MEA electrolytes, MEA completely dominates the solvation shell of Mg^{2+} due to the twofold-stronger solvation power of MEA, even when the concentration of MEA is reduced to 3 MEA per Mg^{2+} . As demonstrated in Figure 4C, DME behave as free (bulk) solvents with the ratio of MEA:Mg varying from 3 to 23.2 (MEA only), while the fraction of bound MEA increases as MEA:Mg decreases, with corresponding trends in the ^{13}C chemical shifts of MEA. By using the temperature-dependent ^{13}C line shape analysis, we can obtain the coordination number and solvent exchange rates of MEA at varying temperatures and MEA concentrations. Due to the “flat” energy landscape of MEA-Mg coordination configurations, the coordination

number of MEA gradually decreases from ~ 5.0 when MEA:Mg ≥ 15 to ~ 3.0 at MEA:Mg of 3 (Figure 4D). At MEA:Mg > 3 , two different ^{13}C signals corresponding to free and “averaged” bound MEA are observed below $-45\text{ }^\circ\text{C}$ (with the latter being the net NMR signal of the accessible configurations averaged over the NMR time scale). The exchange rates between these signals can be calculated using ^{13}C - ^{13}C EXSY at low temperatures and ^{13}C line shape analysis at higher temperatures. At 3 MEA per Mg, two different ^{13}C signals of MEA are also observed at $-45\text{ }^\circ\text{C}$ (Figure S25), but they are both arising from two different configurations of MEA bidentately coordinating to Mg^{2+} , respectively (ascertained by comparing the experimental chemical shifts with MD simulation values in Table S17). The exchange rates between these two forms of coordinating MEA at 3 MEA per Mg is much slower compared to the exchange between free and bound MEA at MEA:Mg > 3 (Figure 4E). The averaged residence time (τ_{res}) of MEA coordinating to Mg^{2+} increasing from $3\text{ }\mu\text{s}$ in neat MEA to $37\text{ }\mu\text{s}$ in 6 MEA:Mg and then further to $370\text{ }\mu\text{s}$ in 3 MEA:Mg. Notably, ^{13}C and ^{19}F NMR relaxation measurements also confirm that the TFSI $^-$ anions do not participate in CIPs and mostly exist as free ions in all solutions with MEA:Mg ≥ 3 (Figure S26), so the possible occurrence of ion aggregates does not constitute a confounding variable for the coordination number determinations.

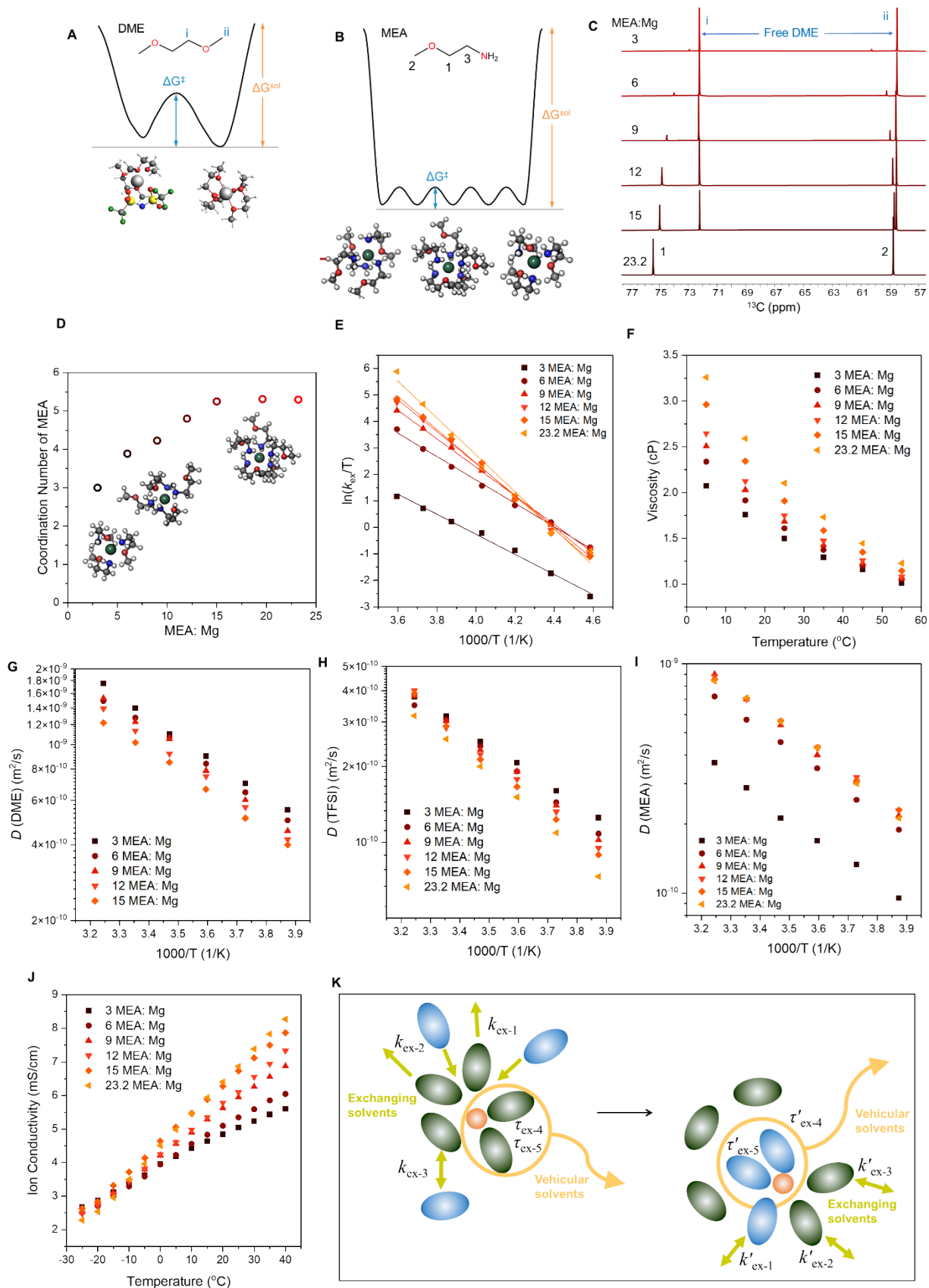


Figure 4. Ion transport is governed by both viscosity and solvent exchange dynamics. The free energy profiles of Mg^{2+} ion solvation in DME (A) and MEA (B), illustrating their differences in solvation structure and solvation exchange dynamics, as the former is decided by solvation energy ΔG^{sol} and the latter by activation barrier ΔG^\ddagger . (C) ^{13}C NMR spectra of 0.45 M MgTFSI_2 in the DME/MEA binary mixtures showing that MEA is the only coordinating solvent. (D) Coordination number of MEA as a function of MEA concentration estimated from variable-temperature ^{13}C NMR spectra. (E) Eyring plots of MEA exchange rates k_{ex} , (F) viscosity, (G) diffusion coefficients obtained from PFG NMR $D(\text{DME})$, (H) $D(\text{TFSI})$, (I) $D(\text{MEA})$, as well as (J) ion conductivity of the electrolytes at varying temperatures. (K) Proposed ion transport mechanism with both vehicular-coordinating solvents and exchanging solvents.

Since DME molecules do not coordinate to Mg in solutions with $\text{MEA}:\text{Mg} \geq 3$ and can be considered as “diluent” molecules in these binary mixtures, the estimated k_{ex} plotted against the concentration of free MEA can be used to determine the rate law and mechanism of solvent exchange: $k_{\text{ex}} = k_1 + k_2 \cdot c_{\text{free solvent}}$. Here, k_1 and k_2 are the rate constants for D- or A-activated exchange process. As shown in Figure S27, k_{ex} increases as the concentration of MEA increases, leading to $k_1 = 11 \times 10^3 \text{ s}^{-1}$ and $k_2 = 36 \times 10^3 \text{ s}^{-1}$ (at 25 °C). The positive and comparable values in k_1 and k_2 indicate that MEA exchange navigates a continuous range of D- and A-activated pathways where both entering and leaving MEA contribute to the transition state. Interestingly, k_{ex} is almost invariant to the MEA concentration at -45 °C when $\text{MEA}:\text{Mg} \geq 6$, suggesting that a stronger contribution of D-activated pathways occurs at lower temperatures.

Turning to the bulk ion transport properties of the electrolytes, the viscosity of the mixture increases with the ratio of $\text{MEA}:\text{Mg}$ (Figure 4F) due to the higher viscosity of MEA as a result of the strong hydrogen-bonding network between intermolecular amine groups, which causes a

decrease in the diffusion coefficients of DME and TFSI⁻ (Figure 4G-H). However, the diffusion coefficients of MEA increase with its concentration in the mixture due to the decreasing fraction of bound MEA, so relative to the NMR time scale, the average MEA diffusion length is longer absent the drag effect of the Mg²⁺ coordination (Figure 4I). Surprisingly, ion conductivity increases with MEA concentration despite the increasing viscosity and the decreasing TFSI⁻ diffusion coefficient (Figure 4J). Because ion pairing is not a concern at MEA:Mg \geq 3, this increase in ion conductivity can be explained by the enhanced Mg²⁺ transport facilitated by the additional MEA. Although changes in the long-range ion correlations between Mg²⁺ and TFSI⁻ may contribute to the change in ion conductivity with MEA:Mg, we do not have experimental evidence of the ion interactions beyond the first solvation shell. On the other hand, the 50% increase in ion conductivity can be correlated to the two orders of magnitude increase in k_{ex} from 3MEA:Mg to 23.2 MEA:Mg at 25 °C: unlike diffusion of TFSI⁻ and DME, which decrease linearly with solution viscosity, diffusion of Mg²⁺ is determined by both k_{ex} and viscosity. A faster k_{ex} prevails over a higher viscosity leading to enhanced cation transport as the MEA concentration increases, because viscosity is reflective of both solvent-solvent and ion-solvent interactions, while solvent exchange dynamics spotlight the ion-solvent interactions.

This picture of cation transport emphasizes the role of solvent exchange, especially for the ions with ultraslow solvent exchange processes where vehicular transport is usually considered to be the major mechanism. In the MEA/DME mixtures, the root-mean-square cation diffusion lengths $\lambda_{\text{rms}} = \sqrt{6D\tau_{\text{res}}}$ are estimated to vary from \sim 550 nm at 3 MEA:Mg to \sim 80 nm at 23.2 MEA:Mg (neat MEA), which are 2 – 3 orders of magnitude greater than the radius of the Mg(MEA)₃₋₆ solvation sheath (5 – 10 Å). Therefore, Mg²⁺ is expected to move with its entire solvating environment as in vehicular transport. However, our results that serve to correlate ion conductivity

and k_{ex} demonstrate that even at the “vehicular diffusion limit”, solvent exchange still contributes remarkably to ion transport, suggesting that ideal vehicular transport is difficult to realize. The actual diffusion mechanism in these multivalent electrolytes is the mixing of both vehicular and structural diffusion (Figure 4K), with some coordinating solvents transporting along with the ions at an averaged residence time and some moving out of the first coordination shell and being replaced by other solvents. The observed solvent exchange rate is the weighted average of all types of solvents. Consequently, the fast solvent exchange process promotes ion transport even at the ultraslow limit.

Desolvation, charge transfer, and the interfacial model

In order to understand the correlation between solvent exchange dynamics and interfacial phenomena, galvanostatic electrochemical impedance spectroscopy (GEIS) was also performed on the MgTFSI₂/MEA/DME electrolytes. In a plating/stripping cycle at a current density of 0.45 mA/cm², the Mg//Mg cell shows a decreasing electrode polarization (defined as the potential difference between plating and stripping plateau, refer to Figure S28) with increasing MEA:Mg ratio, especially when this ratio is above 3. This decreasing electrode polarization is correlated with the reduced τ_{res} of coordinating MEA (Figure 5A). With τ_{res} below 5 μs at MEA:Mg ratios spanning from ~ 12 to 23.2 (neat MEA), the electrode polarization stabilizes below 0.1 V. GEIS spectra also clearly demonstrate a monotonic decrease in charge transfer resistance as MEA:Mg increases (Figure 5B). Moreover, the Bode plots of the impedance spectra at MEA:Mg ratios of 0, 3, and 15 revealed different surface interfacial phenomena in these solutions (Figure 5C). In particular, the mid-frequency region (10^4 - 10^1 Hz), which is generally associated with interfacial phenomena, includes the impedance of charge transfer and surface film formation. With increased

current density, the 0 MEA:Mg cell showed increased electrode impedance, suggesting that the interfacial effect was dominated by the diffusion of Mg^{2+} in the surface layer. The phase angle (Figure S29) is close to 0° , implying resistive behavior. This result also suggested that surface passivation occurred in the DME electrolyte and inhibited the Mg plating/stripping process. At the MEA:Mg ratio of 3, the Bode plots show similar spectra to those without MEA, but the increase in electrolyte impedance with current density is slightly lower (Figure 5D). In contrast, the cell with MEA:Mg of 15 shows decreased electrode impedance at higher current densities (Figure 5E), which suggests that the interfacial effect is dominated by charge transfer. Therefore, the minimization of surface passivation occurs not just by the presence of MEA in the solvation sheath of Mg^{2+} as suggested by Hou et al, but more importantly, by the fast MEA exchange dynamics exhibited at a higher MEA:Mg ratio.¹⁰

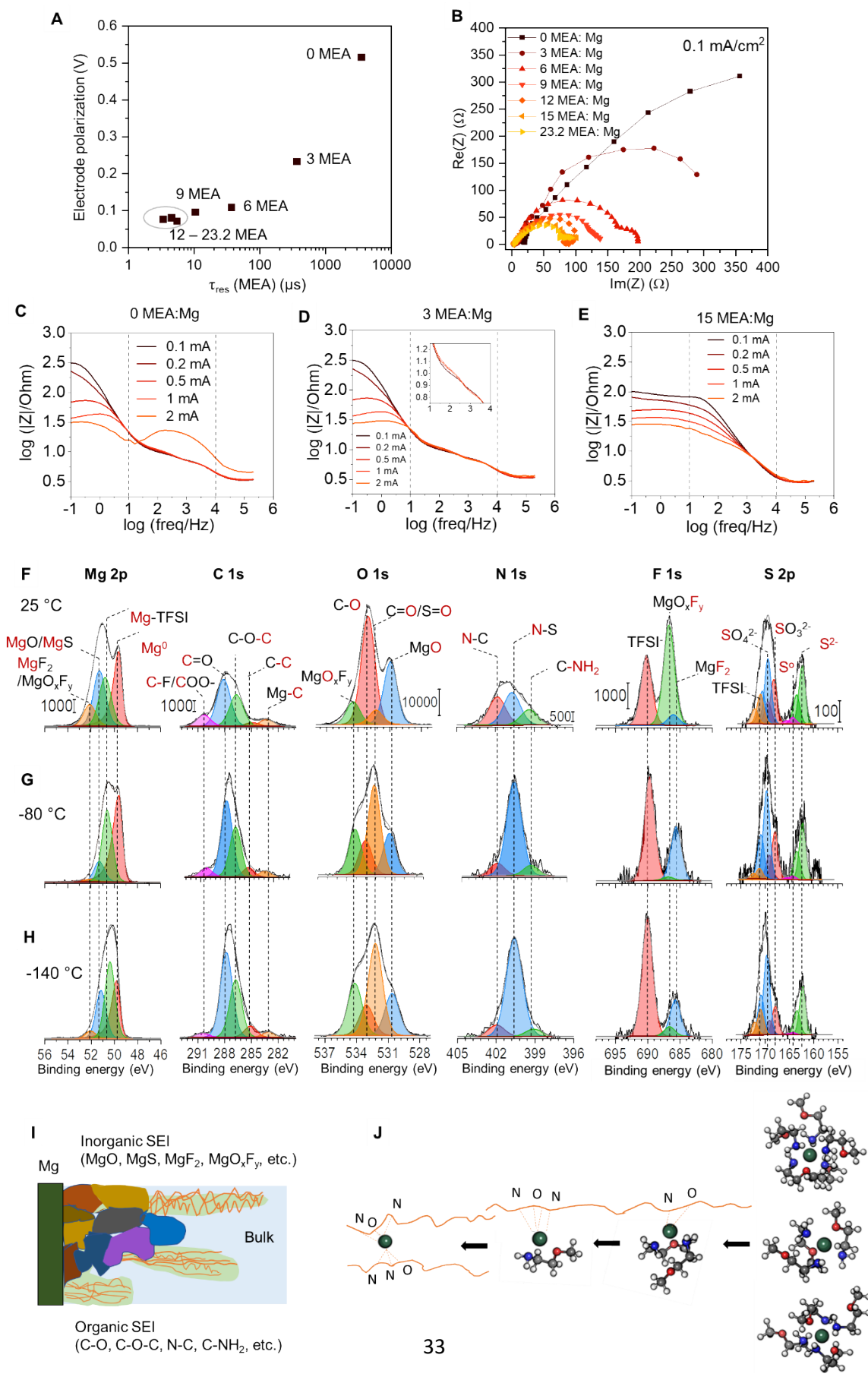


Figure 5. Interfacial properties of Mg electrode in 0.45 M MgTFSI₂ DME/MEA electrolytes. (A) Electrode polarization plotted against the residence time of coordinating MEA. (B) GEIS spectra at varying MEA concentrations. (C-E) Bode plots of impedance spectra at MEA: Mg ratio of 0 (C), 3 (D), and 15 (E). (F-H) Cryo-XPS analysis of Mg electrode after cycling in 0.45 M Mg(TFSI)₂ with 15 MEA/DME solvent at analysis temperatures of (F) -140 °C, (G) - 80 °C, and (H) 25 °C. (I) Proposed interfacial model with organic SEI layers (areas with orange lines) which aid the desolvation process and the inorganic amorphous SEI layers (areas with solid colors) which partially allow the transport of Mg²⁺. (J) Schematic illustration of the desolvation process facilitated by organic SEI via shredding of the coordinating MEA one-by-one as Mg²⁺ moves towards the anode.

Furthermore, the signature of MEA in the composition of the solid electrolyte interphase in an Mg electrode is investigated using cryo-XPS. With this method, the Mg electrode is subjected to the cryogenic state directly after extracting it from the cell and is maintained at cryo-temperature during collection of the XPS spectra. This additional rigor can reveal the composition of the SEI with minimal decomposition of metastable constituents. At -140 °C, the Mg 2p spectrum (Figure 5H) confirms the presence of metallic Mg (49.7 eV binding energy) together with MgO/MgS (51.3 eV), MgF₂/MgO_xF_y (52.1 eV) and residual Mg(TFSI)₂ at 50.8 eV. The formation of surface species such as MgS, MgF₂, and MgO_xF_y originates from the decomposition of TFSI-, which is strongly supported by F 1s, S 2p, and O 1s spectra. In the C 1s spectrum, the dominant signals are C-O-C and C=O species, followed by minor signals of C-C, magnesium carbide, and carboxylate and/or C-F-containing species. The dominance of organic species in the SEI layer is supported by the strong C-O (533 eV) and C=O (532.4 eV) signals in O 1s spectra. In the N 1s spectra, the main

signal at 400.6 eV is attributed to the N-S signature of residual TFSI⁻. The small signals at 399.1 eV and 402 eV are assigned to amine (-NH₂) and C-N species, respectively.

With increasing temperature from -140 °C to -80 °C (Figure 5G) and then 25 °C (Figure 5F), the residual MEA washing solution and volatile components of the SEI evaporate, which is reflected by the decreased intensity of C-O-C and C=O in C 1s spectra and C=O/S=O in the O 1s spectra. The C-O-C signal may originate from both MEA and DME, as both obviously contain ether functional groups. The signal of the TFSI⁻ anion is also slightly reduced, probably due to the loss of TFSI⁻ into the vacuum in concert with the evaporation of other organic species. The evaporation of the residual solvents and organic components intensifies the signal from the inorganic components consisting of metallic Mg in Mg 2p, MgO signal in O 1s, MgO_xF_y and MgF₂ in the F 1s spectra, along with MgS in the S 2p spectra; because more inorganic layers become detectable after the organic surface layers evaporate. Residual gas analyzer (RGA) spectrum of the gas evolution during cryo-XPS (Figure S30) shows that a small amount of MEA and MEA decomposition products are detected when ramping the temperature from -145 °C to -80 °C under vacuum, which originates from the residual washing solution. Furthermore, a substantial amount of MEA and its decomposition products as well as a much smaller amount of DME and TFSI⁻ decomposition products are observed when ramping from -80 °C to 25 °C, confirming that (1) the loosely associated species on SEI layers is lost into the vacuum at room temperature; (2) MEA is the dominating coordinating species to Mg²⁺ instead of DME and TFSI⁻. Remarkably, the N 1s spectra show a significantly increased intensity of N-C and C-NH₂ with the increased temperature, which suggests that the observed species stems from the decomposition of MEA strongly attached to the interface rather than the residual washing solution or loosely associated species. More importantly, these two signals remain strong even after 15h drying under ultra-high vacuum ($\sim 1 \times$

10^{-8} Torr) (Figure S31). In addition, despite the reduced intensity, the organic layers comprised of ether and carboxyl-containing species remain dominant in the SEI layer. Nevertheless, our cryo-XPS results confirm that the SEI is a signature of the primary solvation sheath of the working cation: the solvation of Mg^{2+} with MEA cosolvent modifies the SEI composition as manifested in the presence of amine-containing species and a polyether rich layer, in addition to inorganic MgO , MgF_2 and MgO_xF_y -rich layers.

With the above observations, we propose an interfacial model with an organic-rich layer that facilitates cation desolvation and an inorganic amorphous layer that allows for Mg^{2+} diffusion (Figure 5I); this two-layer model is similar to what has previously been reported for Li-ion batteries.⁵⁶ This model includes a few features which follow as direct consequences of our experimental results: (1) solvent exchange rates in the bulk solution are a good indicator of the initial desolvation process at the early contact between the electrolytes and the outer SEI layer. The ultraslow solvent exchange of $\text{Mg}(\text{DME})_3^{2+}$ with a residence time of 1 – 10 ms may be the main reason for the enormous surface passivation in DME-based electrolytes as other reactions, such as TFSI⁻ decomposition, compete with the desolvation process. By contrast, the much faster solvent exchange of $\text{Mg}(\text{MEA})_n^{2+}$ ($n \sim 3 - 6$) may readily begin the desolvation process at the outer SEI layer, minimizing the influence of other reactions. (2) The outer organic layer containing the decomposition products of organic solvents and anions plays an important role in completing the desolvation of Mg^{2+} . For example, the organic layer containing the asymmetric coordination sites with both nitrogen and oxygen may assist in removing the coordinating MEA one by one as Mg^{2+} diffuses towards the anode. (3) The inorganic layer containing amorphous MgF_2 and MgO_xF_y permits the transport of Mg^{2+} . This model highlights the importance of solvent exchange and desolvation at the interface (Figure 5J), especially for multivalent cations with strong interactions

between ions and solvents. As λ_{rms} can reach hundreds of nanometers in bulk solution with $\tau_{\text{res}}(\text{MEA})$ of 3 – 400 μs , if it is assumed that $D(\text{Mg})$ reduces by an order of magnitude on approaching the interface ($1 \times 10^{-11} \text{ m}^2/\text{s}$), λ_{rms} is 10 – 20 nm with $\tau_{\text{res}}(\text{MEA})$ of 2 – 5 μs . Because the thickness of the SEI has been estimated to be $\sim 20 \text{ nm}$, $\tau_{\text{res}}(\text{solvent})$ must necessarily be less than 10 μs in order to avoid surface passivation. Desolvation otherwise becomes a major rate-limiting step as $\tau_{\text{res}}(\text{solvent})$ increases. The solvent exchange rate may be remarkably smaller in multivalent cations due to their larger charge density. For example, $\tau_{\text{res}}(\text{water})$ is $\sim 10 \text{ ns}$ with charge-dense (but monovalent) Li^+ , compared to $\sim 2 \mu\text{s}$ with Mg^{2+} . Consequently, designing multivalent electrolyte blends with rapid solvent exchange dynamics is a more critical issue to consider in the design of multivalent rechargeable batteries compared with conventional monovalent batteries.

Conclusions

In conclusion, we report a variety of magnesium solvation structures and solvent exchange rates in MgTFSI_2 -3DME-cosolvent and MgTFSI_2 -DME-MEA electrolyte mixtures using multinuclear multimodal NMR methods, supported by MD/DFT calculations, and examine the ramifications for interfacial reactions via GEIS and cryo-XPS. The coordination number of each type of solvent in a mixed-solvent electrolytes is primarily determined by the solvent's donor number, whereas CIP formation is correlated not just to the solvent's donor number, but also the relative permittivity and viscosity for a bulky anion with low charge density such as TFSI⁻.

The residence times of the cosolvents coordinating to Mg^{2+} range from 0.5 μs for TEPC, 3 – 4 μs for MEA and ACN, 30 μs for PC, 360 μs for EiPS up to 3.5 ms for DME at 25 °C, which are 4 –

5 orders of magnitude greater than the previously proposed lower experimental boundary (hundreds of picoseconds) using 2D IR, suggesting that most of the battery-relevant solvents routinely examined for nonaqueous electrolytes exhibit ultraslow solvent exchange. The solvent exchange rates are found to be correlated to the combined effects of coordination steric constraints, solvent rotational freedom, coordination asymmetry, solvent-solvent interaction, solvent mobility, and solvent rearrangement around metal ions.

In dual-solvent MgTFSI₂ electrolytes consisting of both DME and MEA, the solvent exchange rate $k_{\text{ex}}(\text{MEA})$ increases with the molar ratio of MEA per Mg, while DME effectively serves as a diluent to control the MEA:Mg ratio. Ion transport and interfacial properties are found to be clearly correlated to $\tau_{\text{res}}(\text{MEA})$. While the viscosity of the mixed solvents increases with the ratio of MEA:Mg (causing $D(\text{DME})$ and $D(\text{TFSI}^-)$ to decrease), the ionic conductivity surprisingly increases, suggesting that there is enhanced Mg²⁺ transport because ion pairing is minimal at MEA:Mg ≥ 3 . These findings reveal that the ion transport mechanism comprises a mixture of both vehicular and structural diffusion, even at the ultraslow exchange limit. In this picture, some coordinating solvents are transported along with the ions at an averaged τ_{res} and some exchange in and out of the first coordination shell, with the latter fast solvent exchange process leading to enhanced cation transport.

The correlation between electrode polarization and $\tau_{\text{res}}(\text{MEA})$ in the MgTFSI₂-DME-MEA electrolytes, as well as the transition from surface passivation to charge transfer as the dominating interfacial effect at an increasing MEA:Mg ratio, are strong evidence for the link between the rapid solvent exchange dynamics and the performance of the plating/stripping process of magnesium batteries. Our cryo-XPS results demonstrate that the SEI includes both organic-rich regions, with amine-containing and polyether species, and inorganic-rich regions with MgO, MgF₂ and MgO_xF_y.

We therefore propose an interfacial model that highlights the importance of the solvent exchange and the desolvation processes, which can be facilitated by the organic SEI layers working in conjunction with the inorganic layers promoting Mg^{2+} conduction to the electrode surface. We anticipate that the solvent exchange process and its importance in determining ion transport and interfacial properties for rechargeable multivalent batteries will play a central role in the emerging design philosophy that will ultimately yield more energy-dense, reliable, and widely available energy storage platforms.

Supporting Information

This supporting information is available free of charge at

<https://pubs.acs.org/doi/>

Experimental methods including sample preparation, NMR characterization, NMR data analysis, Galvanostatic electrochemical impedance spectroscopy, Cryo-XPS, measurements of viscosity, density, relative permittivity, donor number and ion conductivity, and MD simulations and DFT calculations methods; Examples of 1D and 2D NMR spectra used for solvation structures and solvent exchange dynamics; MD and DFT simulation results; Mg^{2+} solvent/ligand exchange rates reported in literature; NMR, GEIS, and Cryo-XPS results of MgTFSI_2 in the mixed DME and MEA electrolytes.

Acknowledgments

This work was supported by the Joint Center for Energy Storage Research (JCESR), FWP 63076 at PNNL, an Energy Innovation Hub funded by the U.S. Department of Energy, Office of Science, Office of Basic Energy Sciences (BES). A portion of the NMR

experiments were performed with user proposals 50433, 60243 and 60601 at the Environmental Molecular Sciences Laboratory, a DOE Office of Science User Facility sponsored by the Biological and Environmental Research program under Contract No. DE-AC05-76RL01830. Y.C. acknowledges Robert. P. Young for assisting with setting up ^{13}C - ^{13}C EXSY experiments with ^1H decoupling. R.A. acknowledges support via a Junior Research Award from the Institute for Advanced Computational Science (IACS) at Stony Brook University. The authors also acknowledge computing resources from IACS for MD simulations and DFT calculations of the magnesium solvated structures. Sandia National Laboratories is a multimission laboratory managed and operated by National Technology & Engineering Solutions of Sandia, LLC, a wholly owned subsidiary of Honeywell International Inc., for the U.S. Department of Energy's National Nuclear Security Administration under contract DE-NA0003525. This paper describes objective technical results and analysis. Any subjective views or opinions that might be expressed in the paper do not necessarily represent the views of the U.S. Department of Energy or the United States Government.

References

1. Ming, J.; Cao, Z.; Wahyudi, W.; Li, M.; Kumar, P.; Wu, Y.; Hwang, J.-Y.; Hedhili, M. N.; Cavallo, L.; Sun, Y.-K., et al., New Insights on Graphite Anode Stability in Rechargeable Batteries: Li Ion Coordination Structures Prevail over Solid Electrolyte Interphases. *ACS Energy Letters* **2018**, *3*, 335-340.
2. Li, X.; Wang, X.; Ma, L.; Huang, W., Solvation Structures in Aqueous Metal-Ion Batteries. *Adv. Energy Mater* **2022**, *12*, 2202068.
3. Rajput, N. N.; Seguin, T. J.; Wood, B. M.; Qu, X.; Persson, K. A., Elucidating Solvation Structures for Rational Design of Multivalent Electrolytes—a Review. *Top. Curr. Chem.* **2018**, *376*, 19.
4. Cao, X.; Jia, H.; Xu, W.; Zhang, J.-G., Review—Localized High-Concentration Electrolytes for Lithium Batteries. *J. Electrochem. Soc.* **2021**, *168*, 010522.
5. Mao, J.; Wang, C.; Lyu, Y.; Zhang, R.; Wang, Y.; Liu, S.; Wang, Z.; Zhang, S.; Guo, Z., Organic Electrolyte Design for Practical Potassium-Ion Batteries. *Journal of Materials Chemistry A* **2022**, *10*, 19090-19106.

6. Liu, Q.; Yang, G.; Li, X.; Zhang, S.; Chen, R.; Wang, X.; Gao, Y.; Wang, Z.; Chen, L., Polymer Electrolytes Based on Interactions between [Solvent-Li⁺] Complex and Solvent-Modified Polymer. *Energy Storage Materials* **2022**, *51*, 443-452.
7. Tapia-Ruiz, N.; Armstrong, A. R.; Alptekin, H.; Amores, M. A.; Au, H.; Barker, J.; Boston, R.; Brant, W. R.; Brittain, J. M.; Chen, Y., et al., 2021 Roadmap for Sodium-Ion Batteries. *Journal of Physics: Energy* **2021**, *3*, 031503.
8. Zhang, Q.; Ma, Y.; Lu, Y.; Zhou, X.; Lin, L.; Li, L.; Yan, Z.; Zhao, Q.; Zhang, K.; Chen, J., Designing Anion-Type Water-Free Zn²⁺ Solvation Structure for Robust Zn Metal Anode. *Angew. Chem. Int. Ed.* **2021**, *60*, 23357-23364.
9. Cao, L.; Li, D.; Hu, E.; Xu, J.; Deng, T.; Ma, L.; Wang, Y.; Yang, X.-Q.; Wang, C., Solvation Structure Design for Aqueous Zn Metal Batteries. *Journal of the American Chemical Society* **2020**, *142*, 21404-21409.
10. Hou, S.; Ji, X.; Gaskell, K.; Wang, P.-f.; Wang, L.; Xu, J.; Sun, R.; Borodin, O.; Wang, C., Solvation Sheath Reorganization Enables Divalent Metal Batteries with Fast Interfacial Charge Transfer Kinetics. *Science* **2021**, *374*, 172-178.
11. Cheng, H.; Sun, Q.; Li, L.; Zou, Y.; Wang, Y.; Cai, T.; Zhao, F.; Liu, G.; Ma, Z.; Wahyudi, W., et al., Emerging Era of Electrolyte Solvation Structure and Interfacial Model in Batteries. *ACS Energy Letters* **2022**, *7*, 490-513.
12. Lassègues, J.-C.; Grondin, J.; Aupetit, C.; Johansson, P., Spectroscopic Identification of the Lithium Ion Transporting Species in Litfsi-Doped Ionic Liquids. *J. Phys. Chem. A* **2009**, *113*, 305-314.
13. Watkins, T.; Buttry, D. A., Determination of Mg²⁺ Speciation in a Tfsi--Based Ionic Liquid with and without Chelating Ethers Using Raman Spectroscopy. *J. Phys. Chem. B* **2015**, *119*, 7003-7014.
14. Hu, J. Z.; Rajput, N. N.; Wan, C.; Shao, Y.; Deng, X.; Jaegers, N. R.; Hu, M.; Chen, Y.; Shin, Y.; Monk, J., et al., 25mg Nmr and Computational Modeling Studies of the Solvation Structures and Molecular Dynamics in Magnesium Based Liquid Electrolytes. *Nano Energy* **2018**, *46*, 436-446.
15. Lapidus, S. H.; Rajput, N. N.; Qu, X.; Chapman, K. W.; Persson, K. A.; Chupas, P. J., Solvation Structure and Energetics of Electrolytes for Multivalent Energy Storage. *Physical Chemistry Chemical Physics* **2014**, *16*, 21941-21945.
16. Salama, M.; Shterenberg, I.; Gizbar, H.; Eliaz, N. N.; Kosa, M.; Keinan-Adamsky, K.; Afri, M.; Shimon, L. J. W.; Gottlieb, H. E.; Major, D. T., et al., Unique Behavior of Dimethoxyethane (Dme)/Mg(N(So2cf3)2)2 Solutions. *J. Phys. Chem. C* **2016**, *120*, 19586-19594.
17. Salama, M.; Shterenberg, I.; J.W. Shimon, L.; Keinan-Adamsky, K.; Afri, M.; Gofer, Y.; Aurbach, D., Structural Analysis of Magnesium Chloride Complexes in Dimethoxyethane Solutions in the Context of Mg Batteries Research. *J. Phys. Chem. C* **2017**, *121*, 24909-24918.
18. Rips, I.; Klafter, J.; Jortner, J., Dynamics of Ionic Solvation. *J. Chem. Phys.* **1988**, *88*, 3246-3252.
19. Helm, L.; Merbach, A. E., Water Exchange on Metal Ions: Experiments and Simulations. *Coord. Chem. Rev.* **1999**, *187*, 151-181.
20. Dunand, F. A.; Helm, L.; Merbach, A. E., Solvent Exchange on Metal Ions. In *Adv. Inorg. Chem.*, Academic Press: 2003; Vol. 54, pp 1-69.
21. Helm, L.; Merbach, A. E., Inorganic and Bioinorganic Solvent Exchange Mechanisms. *Chem. Rev.* **2005**, *105*, 1923-1960.
22. Tanada, K.-i.; Hashimoto, A.; Tsuji, H.; Kato, K.; Inada, Y.; Aizawa, S.-i.; Funahashi, S., Mechanistic Study of Solvent Exchange Reactions of Manganese(II), Iron(II), Nickel(II), Copper(II), and Iron(III) Ions in Bulky 1,1,3,3-Tetramethylurea (Tmu) Solvent by Measurements of Oxygen-17 Nmr Relaxation Rates and Chemical Shifts: Complexation Reaction of Nickel(II) Ion in Tmu and Crystal Structure of [Ni(Tmu)5](Bph4)2. *Inorg. Chim. Acta* **2006**, *359*, 511-518.
23. Hubbard, C. D.; van Eldik, R., Mechanistic Studies of Reactions of Coordination Compounds. Some Recent Highlights. *J. Coord. Chem.* **2007**, *60*, 1-51.

24. Pasgreta, E.; Puchta, R.; Galle, M.; van Eikema Hommes, N.; Zahl, A.; van Eldik, R., Ligand-Exchange Processes on Solvated Lithium Cations: DmsO and Water/DmsO Mixtures. *ChemPhysChem* **2007**, *8*, 1315-1320.
25. Dereka, B.; Lewis, N. H. C.; Zhang, Y.; Hahn, N. T.; Keim, J. H.; Snyder, S. A.; Maginn, E. J.; Tokmakoff, A., Exchange-Mediated Transport in Battery Electrolytes: Ultrafast or Ultraslow? *Journal of the American Chemical Society* **2022**, *144*, 8591-8604.
26. Chen, Y.; Jaegers, N. R.; Wang, H.; Han, K. S.; Hu, J. Z.; Mueller, K. T.; Murugesan, V., Role of Solvent Rearrangement on Mg²⁺ Solvation Structures in Dimethoxyethane Solutions Using Multimodal Nmr Analysis. *J. Phys. Chem. L* **2020**, *11*, 6443-6449.
27. Chen, Y.; Atwi, R.; Han, K. S.; Ryu, J.; Washton, N. M.; Hu, J. Z.; Rajput, N. N.; Mueller, K. T.; Murugesan, V., Role of a Multivalent Ion–Solvent Interaction on Restricted Mg²⁺ Diffusion in Dimethoxyethane Electrolytes. *J. Phys. Chem. B* **2021**, *125*, 12574-12583.
28. Wahyudi, W.; Ladelta, V.; Tsetseris, L.; Alsabban, M. M.; Guo, X.; Yengel, E.; Faber, H.; Adilbekova, B.; Seitekhan, A.; Emwas, A.-H., et al., Lithium-Ion Desolvation Induced by Nitrate Additives Reveals New Insights into High Performance Lithium Batteries. *Adv. Funct. Mater.* **2021**, *31*, 2101593.
29. Li, Q.; Cao, Z.; Wahyudi, W.; Liu, G.; Park, G.-T.; Cavallo, L.; Anthopoulos, T. D.; Wang, L.; Sun, Y.-K.; Alshareef, H. N., et al., Unraveling the New Role of an Ethylene Carbonate Solvation Shell in Rechargeable Metal Ion Batteries. *ACS Energy Letters* **2021**, *6*, 69-78.
30. Zou, Y.; Cao, Z.; Zhang, J.; Wahyudi, W.; Wu, Y.; Liu, G.; Li, Q.; Cheng, H.; Zhang, D.; Park, G.-T., et al., Interfacial Model Deciphering High-Voltage Electrolytes for High Energy Density, High Safety, and Fast-Charging Lithium-Ion Batteries. *Adv. Mater.* **2021**, *33*, 2102964.
31. Lee, S. H.; Hwang, J.-Y.; Ming, J.; Cao, Z.; Nguyen, H. A.; Jung, H.-G.; Kim, J.; Sun, Y.-K., Toward the Sustainable Lithium Metal Batteries with a New Electrolyte Solvation Chemistry. *Adv. Energy Mater* **2020**, *10*, 2000567.
32. Chang, Z.; Qiao, Y.; Yang, H.; Deng, H.; Zhu, X.; He, P.; Zhou, H., Beyond the Concentrated Electrolyte: Further Depleting Solvent Molecules within a Li⁺ Solvation Sheath to Stabilize High-Energy-Density Lithium Metal Batteries. *Energy & Environmental Science* **2020**, *13*, 4122-4131.
33. Chen, Y.; Ryu, J.; Bazak, J. D.; Nguyen, D. T.; Han, K. S.; Li, Z.; Hu, J. Z.; Mueller, K. T.; Murugesan, V., Ion Solvation-Driven Liquid–Liquid Phase Separation in Divalent Electrolytes with Miscible Organic Solvents. *J. Phys. Chem. C* **2023**, *127*, 15443-15453.
34. Bain, A. D., Chemical Exchange in Nmr. *Prog. Nucl. Magn. Reson. Spectrosc.* **2003**, *43*, 63-103.
35. Mann, B. E., Dynamic ¹³C Nmr Spectroscopy. *Prog. Nucl. Magn. Reson. Spectrosc.* **1977**, *11*, 95-114.
36. Eyring, H., The Activated Complex in Chemical Reactions. *J. Chem. Phys.* **1935**, *3*, 107-115.
37. Laidler, K. J.; King, M. C., Development of Transition-State Theory. *J. Phys. Chem.* **1983**, *87*, 2657-2664.
38. Herstedt, M.; Smirnov, M.; Johansson, P.; Chami, M.; Grondin, J.; Servant, L.; Lassègues, J. C., Spectroscopic Characterization of the Conformational States of the Bis(Trifluoromethanesulfonyl)Imide Anion (Tfsi⁻). *J. Raman Spectrosc* **2005**, *36*, 762-770.
39. Matson, G. B., Methyl Nmr Relaxation: The Effects of Spin Rotation and Chemical Shift Anisotropy Mechanisms. *J. Chem. Phys.* **1977**, *67*, 5152-5161.
40. Hahn, N. T.; Kamphaus, E. P.; Chen, Y.; Murugesan, V.; Mueller, K. T.; Cheng, L.; Zavadil, K. R., Magnesium Battery Electrolytes with Improved Oxidative Stability Enabled by Selective Solvation in Fluorinated Solvents. *ACS Applied Energy Materials* **2023**, *6*, 3264-3277.
41. Gutmann, V., *Coordination Chemistry in Non-Aqueous Solutions*; Springer Vienna, 1968, p 174.
42. Chen, J.; Zhang, H.; Fang, M.; Ke, C.; Liu, S.; Wang, J., Design of Localized High-Concentration Electrolytes Via Donor Number. *ACS Energy Letters* **2023**, *8*, 1723-1734.

43. Richens, D. T., Ligand Substitution Reactions at Inorganic Centers. *Chem. Rev.* **2005**, *105*, 1961-2002.
44. Atwi, R.; Chen, Y.; Han, K. S.; Mueller, K. T.; Murugesan, V.; Rajput, N. N., An Automated Framework for High-Throughput Predictions of Nmr Chemical Shifts within Liquid Solutions. *Nature Computational Science* **2022**, *2*, 112-122.
45. Bleuzen, A.; Pittet, P.-A.; Helm, L.; Merbach, A. E., Water Exchange on Magnesium(II) in Aqueous Solution: A Variable Temperature and Pressure ^{17}O Nmr Study. *Magn. Reson. Chem.* **1997**, *35*, 765-773.
46. Nakamura, S.; Meiboom, S., Proton Magnetic Resonance Studies of the Solvation Shell of Mg^{2+} in Methanol. Solvation Number and Exchange Rate. *Journal of the American Chemical Society* **1967**, *89*, 1765-1772.
47. Alger, T. D., Proton Magnetic Resonance Studies of Magnesium(II) in Ethanol. Determination of Solvation Number and Exchange Rate. *Journal of the American Chemical Society* **1969**, *91*, 2220-2224.
48. Dickert, F. L., ^1H and ^{13}C Nmr-Spectroscopic Studies on Acetone Exchange of Nickel and Magnesium Ions. *Berichte der Bunsengesellschaft für physikalische Chemie* **1979**, *83*, 593-596.
49. Pisaniello, D.; Lincoln, S., A Proton Magnetic Resonance Study of Ligand Exchange on the Hexakis-(N, N-Dimethylformamide)Magnesium(II) Ion. *Aust. J. Chem.* **1979**, *32*, 715-718.
50. Dickert, F. L.; Waidhas, M. F., Solvent Exchange on Magnesium([15]Crown-5) Complexes—a First- and Second-Order Reaction. *Angewandte Chemie International Edition in English* **1985**, *24*, 575-576.
51. Pisaniello, D.; Lincoln, S. F.; Williams, E. H., The Exchange of Trimethylphosphate on Magnesium(II). A Phosphorus-31 Nuclear Magnetic Resonance Study. *Inorg. Chim. Acta* **1978**, *31*, 237-240.
52. Pisaniello, D. L. The Dynamics of Ligand Exchange Processes on Magnesium (II), Scandium (III) and Yttrium (III) Ions. University of Adelaide, 1980.
53. Chisholm, M. H.; Choojun, K.; Chow, A. S.; Fraenkel, G., Molecular Dynamics and Ligand Exchange in Magnesium Complexes: Evidence for Both Dissociative and Associative Ligand Exchange. *Angew. Chem. Int. Ed.* **2013**, *52*, 3264-3266.
54. Baskin, A.; Prendergast, D., “Ion Solvation Spectra”: Free Energy Analysis of Solvation Structures of Multivalent Cations in Aprotic Solvents. *J. Phys. Chem. L* **2019**, *10*, 4920-4928.
55. Baskin, A.; Prendergast, D., Ion Solvation Engineering: How to Manipulate the Multiplicity of the Coordination Environment of Multivalent Ions. *J. Phys. Chem. L* **2020**, *11*, 9336-9343.
56. Zhou, Y.; Su, M.; Yu, X.; Zhang, Y.; Wang, J.-G.; Ren, X.; Cao, R.; Xu, W.; Baer, D. R.; Du, Y., et al., Real-Time Mass Spectrometric Characterization of the Solid–Electrolyte Interphase of a Lithium-Ion Battery. *Nature Nanotechnology* **2020**, *15*, 224-230.

TOC

